4. Effect of Microstructure and Texture on Mechanical and Ballistic Properties of AA 7017 Alloy Plate

4.1. Introduction

This chapter deals with the understanding of the ballistic behavior of a 70 mm thick AA-7017 plate in L, LT and ST directions. Related damage patterns of the material after ballistic impact have been analyzed. A comparative study of the microstructure and crystallographic texture has also been carried out in the three directions to understand the difference in ballistic behavior of the material. Quasi-static mechanical properties have been evaluated along the three directions. The ballistic behavior of the material with corresponding microstructure, texture and static mechanical properties along three directions has been correlated.

4.2. Results

4.2.1. Initial microstructure

Triplanar optical microstructure representing three sample directions of the as-received AA-7017 alloy plate is shown in Fig. 4.1a. Owing to rolling, the grain morphology is different along the three sample directions. As displayed by the optical micrograph, the grains of this alloy in the untested condition are found to be pancake shaped and aligned in the rolling direction of the plate. The grain structures are quite different in all the three sample directions in terms of aspect ratios. The microstructure has low aspect ratio grains along ST.

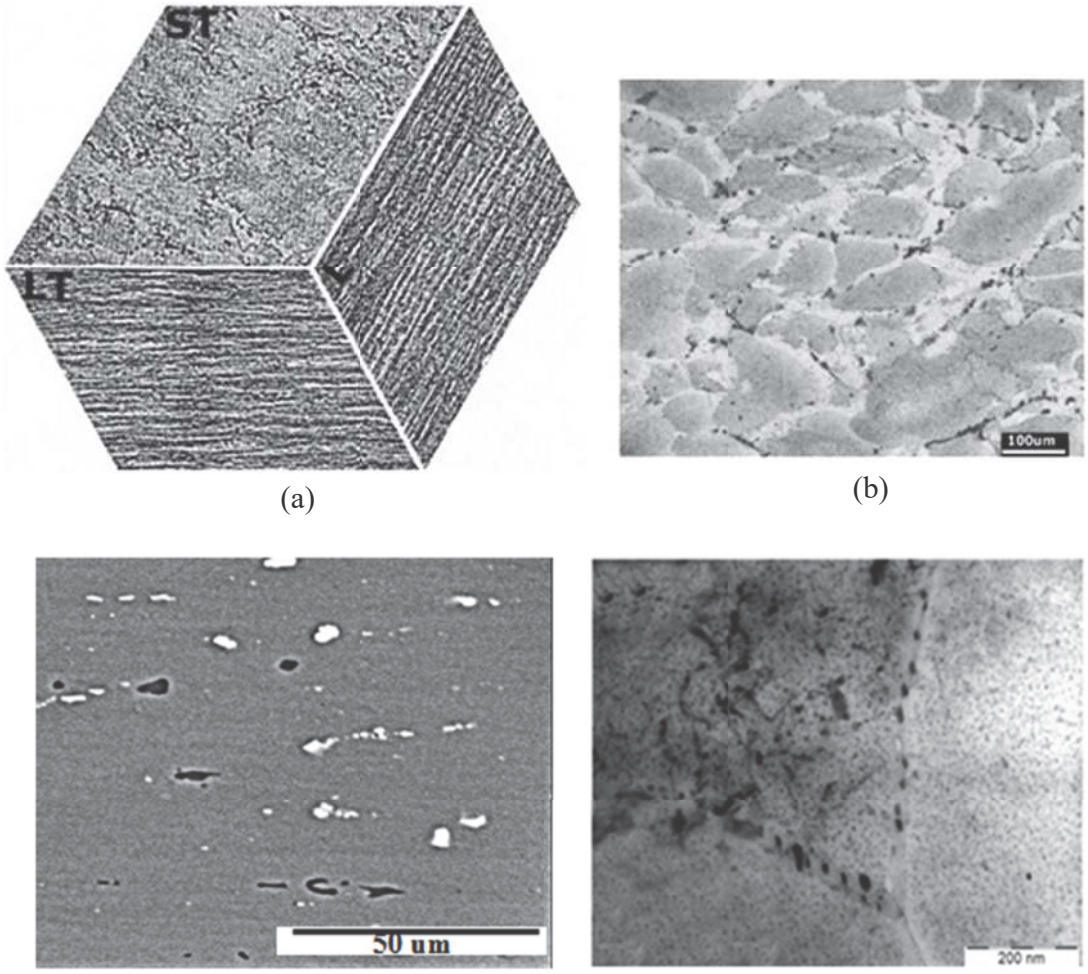

(a) (b)

(c) (d)

Figure 4.1: (a) Triplanar optical microstructure of the as-received AA-7017 alloy, (b) Recrystallized grains in ST direction, (c) Back scattered electron (BSE) microstructure displaying the distributions of intermetallic particles and (d) TEM micrographs illustrating coarse intermetallic particles at the grain boundary.

The high aspect ratio of deformed grains is seen along L and LT. Particle simulated nucleated (PSN) and recrystallized grains are observed along ST (Fig 4.1b). The distribution ofintermetallic particles present in AA-7017 alloy is displayed in Fig. 4.1c. Three typesof particles have been reported in aluminium alloys. These are coarse "constitutive" particles composed of major alloying and impurity elements, partially soluble "dispersoid" particles employed to control grain size and the finer hardening phase particles known as "precipitates". Presence of two types of intermetallic constitutive precipitates with bright and dark contrast is observed in the present alloy (Fig 4.1c). These are Al_6FeMn and Mg_2Si precipitates based on EPMA analysis. Al_6FeMn particles arealso reported by Millet et al. (2004) in AA-7017 alloy. Presence of Al_3Zr dispersoid particles and $MgZn_2$ precipitates in AA-7017 alloy has been reported by Rout et al. (2015). The microstructure observed in TEM is presented in Fig 4.1d. It contains a high density of precipitates in the interior of the grains since this alloy is received in peak aged condition. The precipitates are either round or rod shaped. In addition, intermetallic particles are observed along the grain boundaries.

4.2.2. Texture characterization

The texture of the material in terms of orientation distribution functions (ODF) along three different directions is shown in Fig. 4.2a-c. There is a variation in the overall texture intensity observed along the three directions. The maximum texture intensities along the ST, LT and L directions are 3.8, 28.2 and 38.43 times random, respectively. The major texture components for ST, LT and L directions are {0 1 11}⟨3 11 1⟩ [f(g) =1.9], {0 1 11}⟨15 11 1⟩[f(g)=2.5], {0 1 11}⟨8 11 1⟩[f(g)=2.4], {2 0 3}⟨3 0 2⟩[f(g)=2.0], {1 1 4}⟨2 6 1⟩[f(g)= 3.5], {1 1 3}⟨0 3 1⟩[f(g)=2.9], {2 2 1}⟨3 4 2⟩[f(g)=3.3], {1 1 2}⟨1 1 0⟩ [f(g)=3.4]; {203}⟨302⟩ [f(g)=1.9], {0111}⟨2111⟩ [f(g)=2.45], {115}⟨051⟩ [f(g)=2.4], {111}⟨101⟩ [f(g)=28.2], {665}⟨6116⟩ [f(g)=22.0] and {0 1 11}⟨1 11 1⟩ [f(g)=2.4], {113}⟨031⟩ [f(g)=2.7], {223}⟨032⟩ [f(g)=3.0], {112}⟨311⟩ [f(g)=37.8], {111}⟨121⟩ [f(g)=6.8], respectively. The corresponding typical β fibers of this alloy on three directions are shown in Fig 4.3. The β fibre is very weak in ST while highly inhomogeneous with very high intensity between {112}⟨111⟩ and {123}⟨634⟩ locations in L and LT direction.

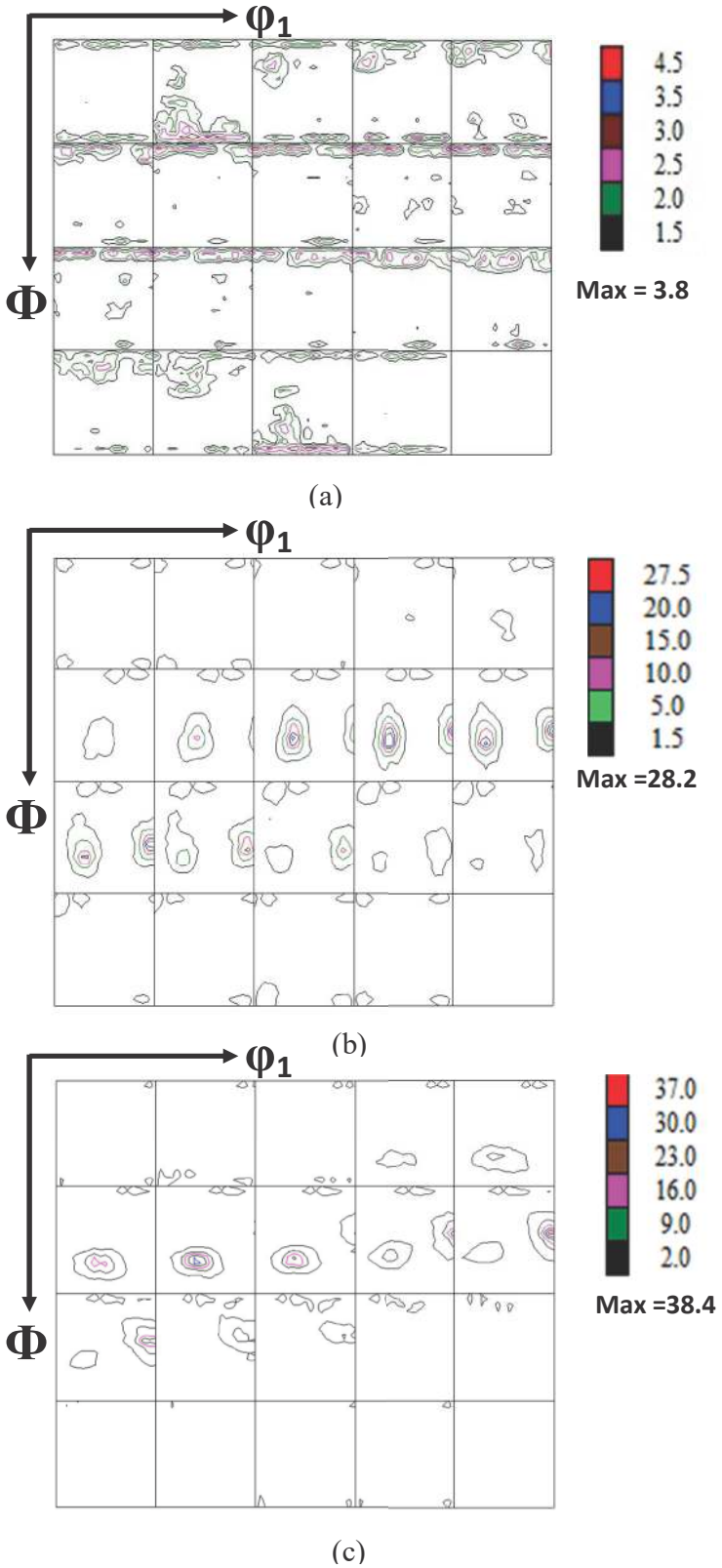

Fig. 4.2: Texture of the plate measured in (a) ST (b) LT and (c) L direction.

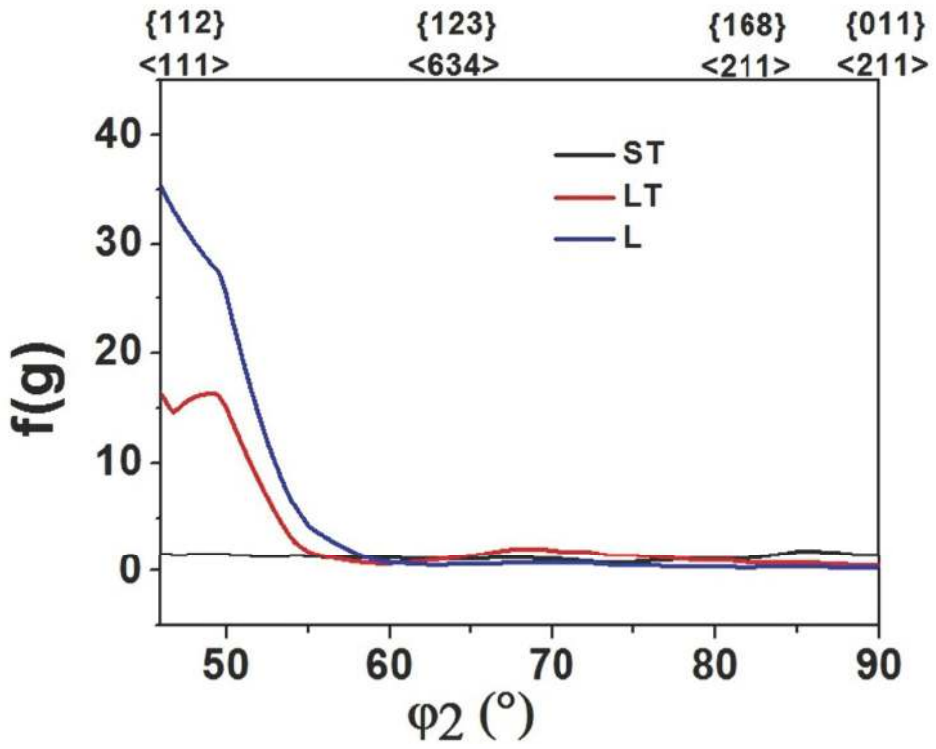

Fig. 4.3 : Typical β fibres in L, LT and ST directions of the plate.

4.2.3. Mechanical properties

Figures 4.4(a, b) show the representative engineering stress-strain and true stress–strain curves for the L, LT and ST direction of the AA-7017 plate. The corresponding average values of σ_{YS}, σ_{UTS} and percentage elongation are plotted in Fig 4.5. It can be seen that highest strength is observed along LT direction. The elongation is seen to be the highest and the lowest along L and ST directions, respectively. The impact energy values obtained from Charpy impact tests are also included in Fig 4(c). The L and ST direction samples show the highest (8 J) and lowest (2 J) impact energy values, respectively.

The SEM fractographs of the broken Charpy impact fracture surfaces are shown in Fig. 4.6a to illustrate the anisotropic fracture mechanism. The fracture features of impact specimens along three directions display a distinctive variation in mode of fracture. The L and LT samples exhibit dimples of varying sizes in the fracture surface with delamination and secondary cracks along the grain boundary. Both the extent of secondary cracks and delamination are more severe in LT direction. In addition, voids are also observed to contain

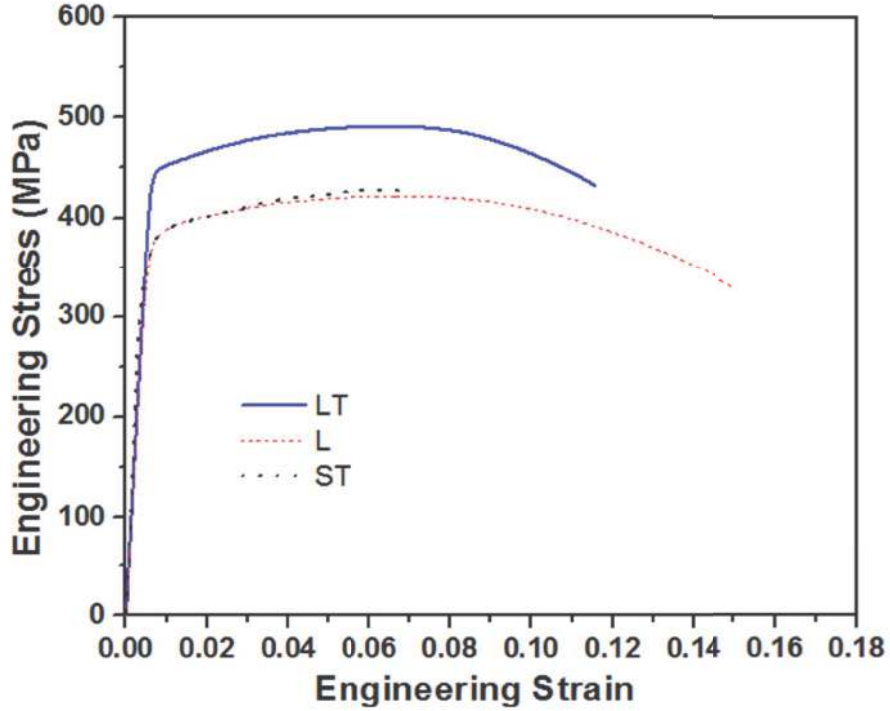

(a)

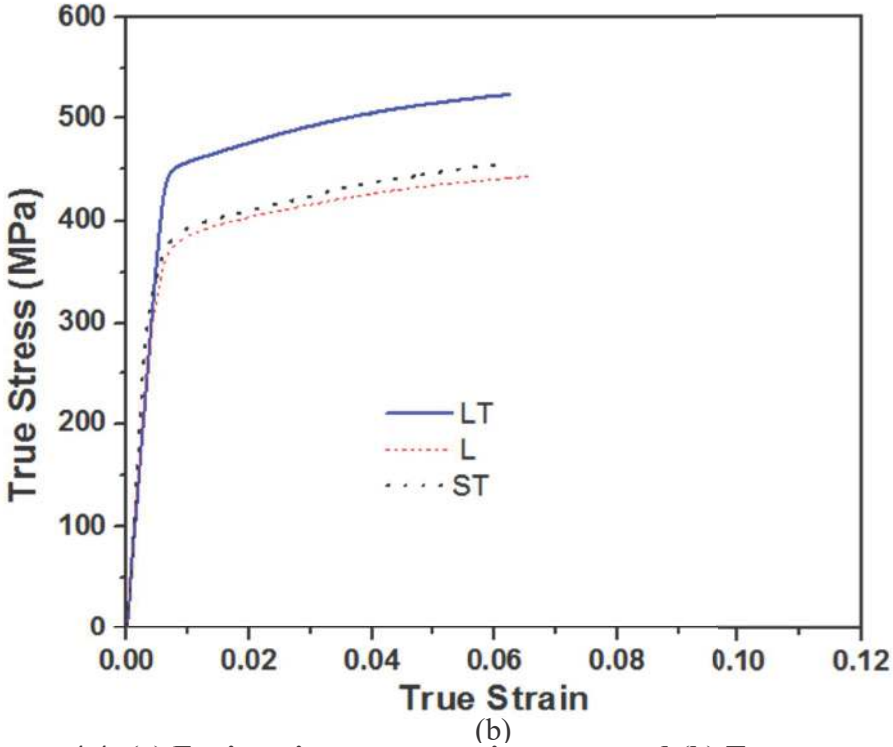

(b)

Figure 4.4: (a) Engineering stress- strain curves and (b) True stress-strain curves along L, LT and ST direction of the AA 7017 plate.

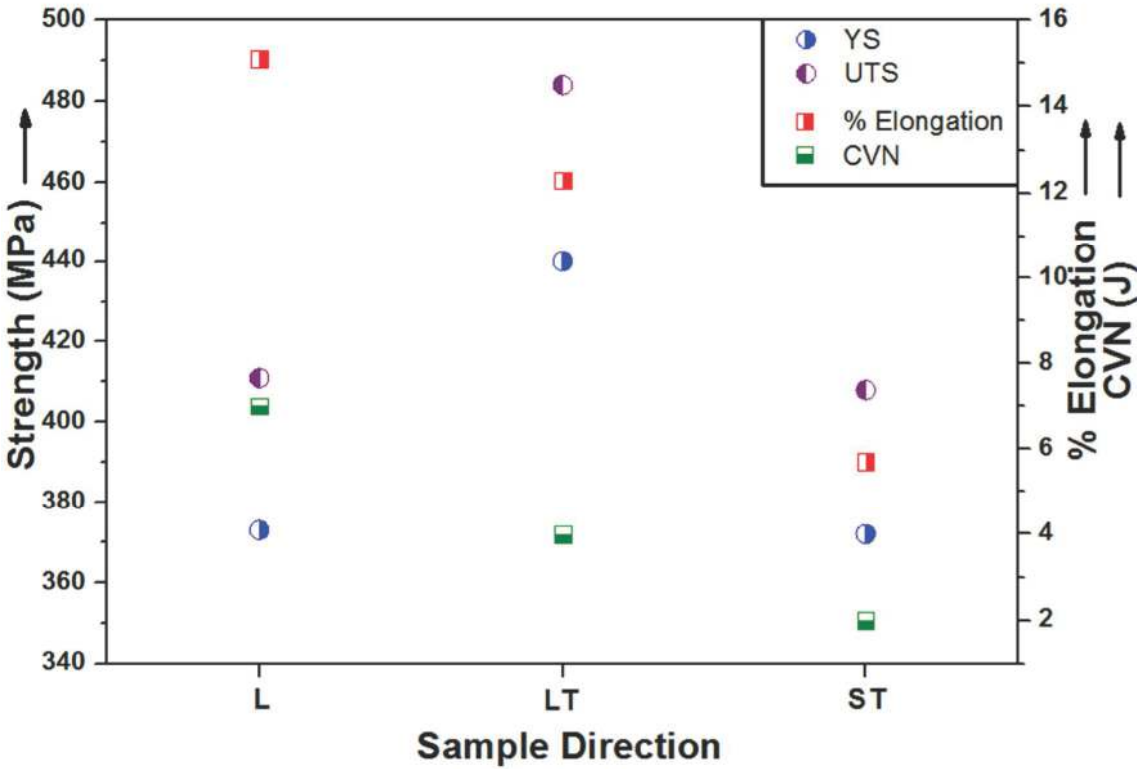

Figure 4.5: Mechanical properties along L, LT and ST direction of the AA-7017 plate.

coarse intermetallic particles. The energy dispersive analysis of X-rays (EDAX) confirms that these particles are Al_6FeMn precipitates (Fig. 4.6b). The fracture surface of ST sample exhibits a slant type failure pattern with large number of intermetallic particles impinge on the voids.

4.2.4. Ballistic evaluation

Ballistic evaluation is carried out on 70 mm thickness plates by impacting with 7.62 mm AP projectiles. The depth of penetration (DOP) values of the ballistically evaluated specimens is depicted in Fig. 4.7. The ballistic resistance in ST direction is higher than those of L and LT, respectively. The visual comparison of the front side of the plates after ballistic evaluation is shown in Fig. 4.8. The material flows out to form perfect petalling damage pattern in the ST direction impacted plates. Partial broken petalling damage is observed in

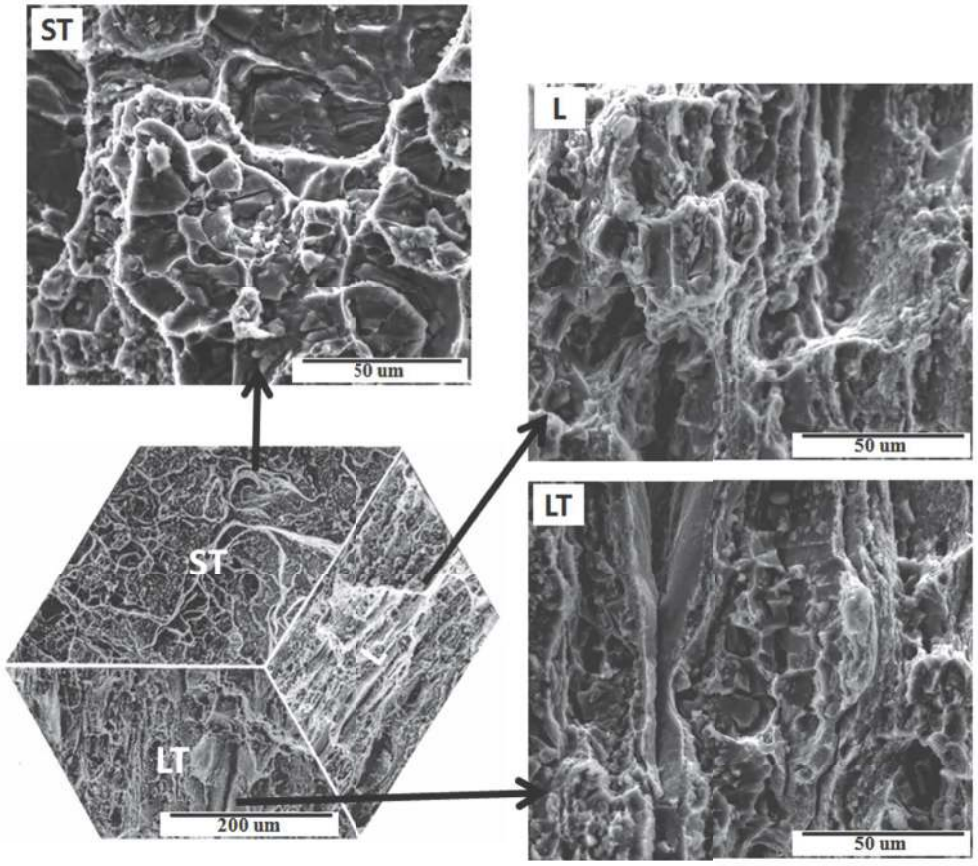

(a)

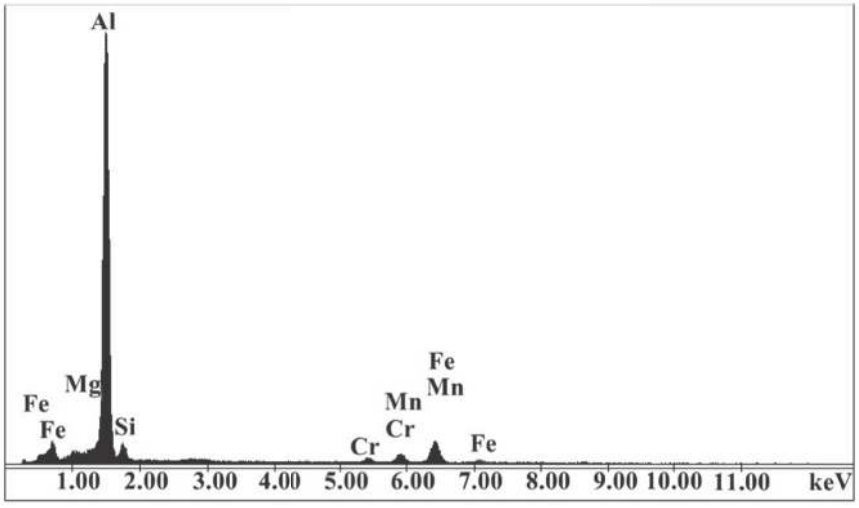

(b)

Figure 4.6: (a) Triplanar SEM fractographs of the broken Charpy impact fracture surfaces represent the anisotropic fracture mechanism and (b) EDAX analysis of the particles present in the fracture surface.

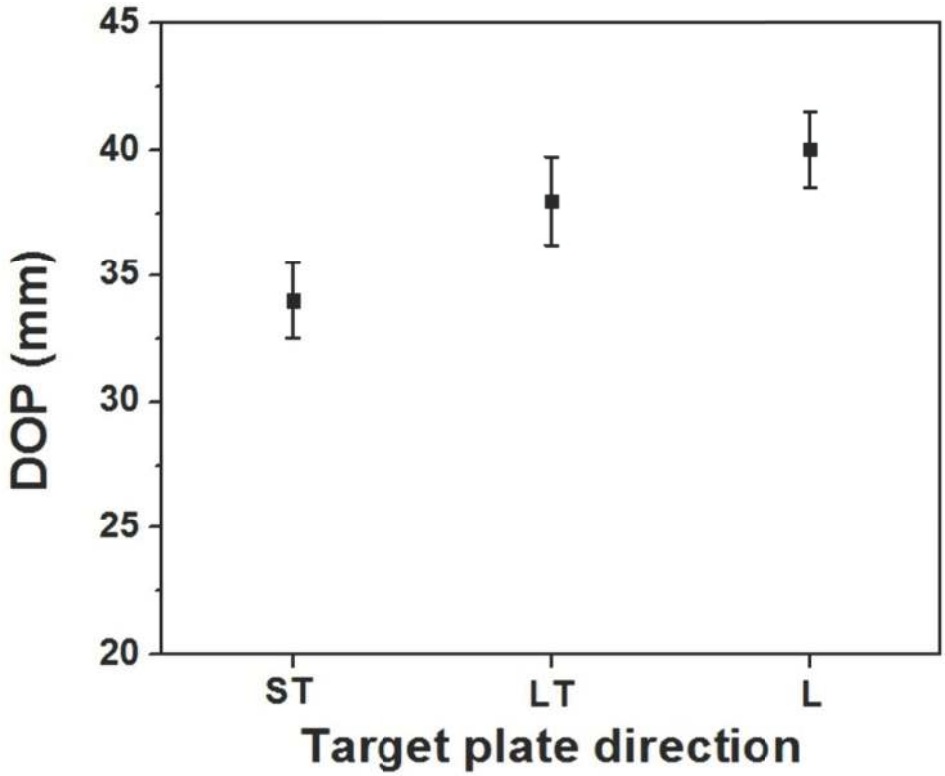

Figure 4.7: Ballistic results in terms of depth of penetration in three directions of the AA-7017 plate.

the front face of LT and L direction impacted plates. It is to be noted here that cracks are seen originating from the impact zones in L and LT direction impacted plates. On the other hand, no cracks are observed in ST direction impacted plates. Small cracks are also observed adjacent to the crater wall in L direction impacted plates after cutting halves of craters subsequent to ballistic impact (Fig. 4.9).

The impact craters (penetration channels) are polished and examined in detail to observe changes in microstructure after ballistic impact. These are mainly focused on adjacent to the crater walls and at the bottom of the crater to find out flow patterns of the material and micro-cracks. Fig. 4.10 shows the microstructure of impacted target plates adjacent to the crater wall. The microstructure of the ST direction impacted plates displays material flow lines severely bent towards the direction of penetration (Fig. 4.10(a)). This phenomenon occurs due to the high material deformation caused by the projectile impact

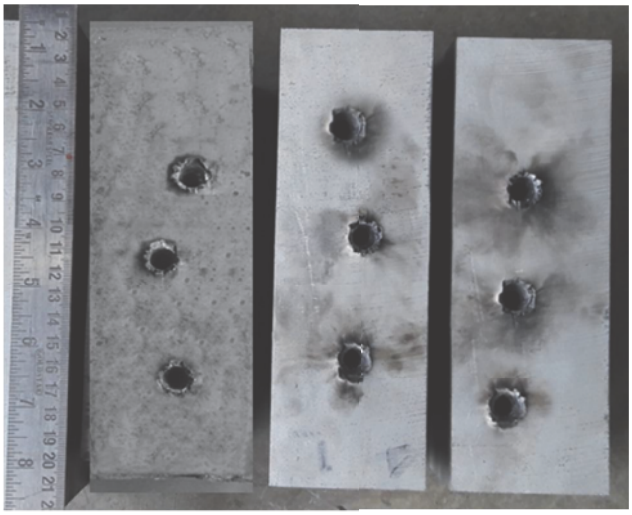

(a)

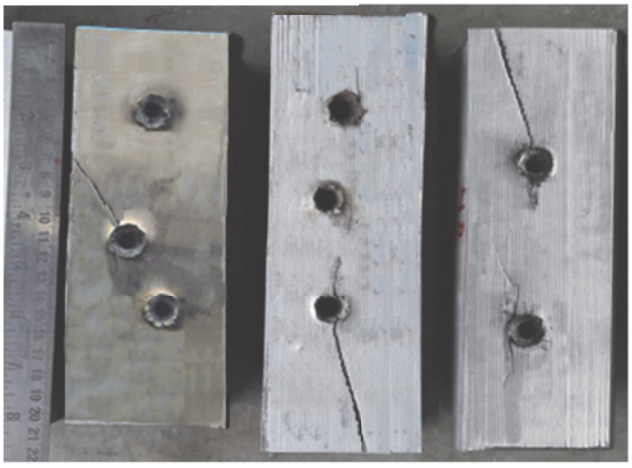

(b)

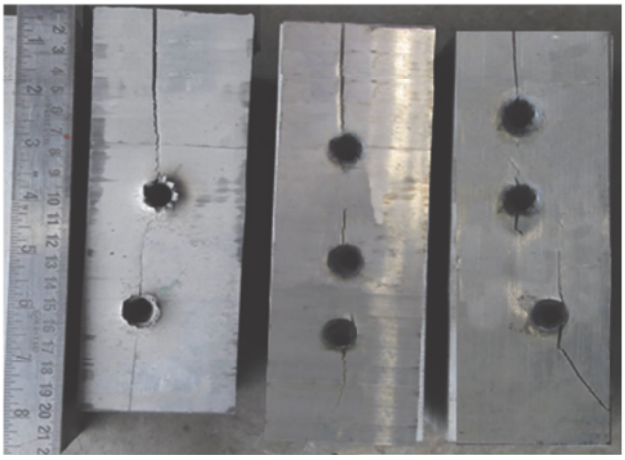

(c)

Fig. 4.8: Front view of the impacted plates in (a) ST (b) LT and (c) L directions after ballistic testing.

Fig 4.9: Half section views of the (i) ST (ii) LT and (iii) L direction impacted craters

[Manes et al., 2014]. This sample does not show the presence of micro cracks throughout the crater. On the other hand, the microstructures of the L and LT direction impacted plates display very little material flow adjacent to the crater wall (Fig. 4.10(b-c)). In addition, these samples show the presence of micro cracks which are emanating out from the crater wall. At the bottom of the crater in the ST direction impacted plates, well defined and smooth material flow lines are observed (Fig. 4.10(d)). In contrast, severely deformed grains are seen at the bottom of craters formed in the L and LT impacted plates (Fig.4.10(e-f)).

Micro-hardness values close to the bottom of the crater have been plotted as function of distance in order to understand the deformation behavior. The variation in hardness values for craters formed by the projectile impact is summarized in Fig.4 11. It can be noticed that in case of craters formed in L direction impacted plates, the increase in hardness is observed upto approximately 6 mm from the crater wall. Whereas, in case of craters formed in the LT and ST direction impacted plates, the increase in hardness is observed approximately up to 15 mm from the crater wall. However, the extent of increase in hardness is higher in case of craters formed in ST direction impacted targets.

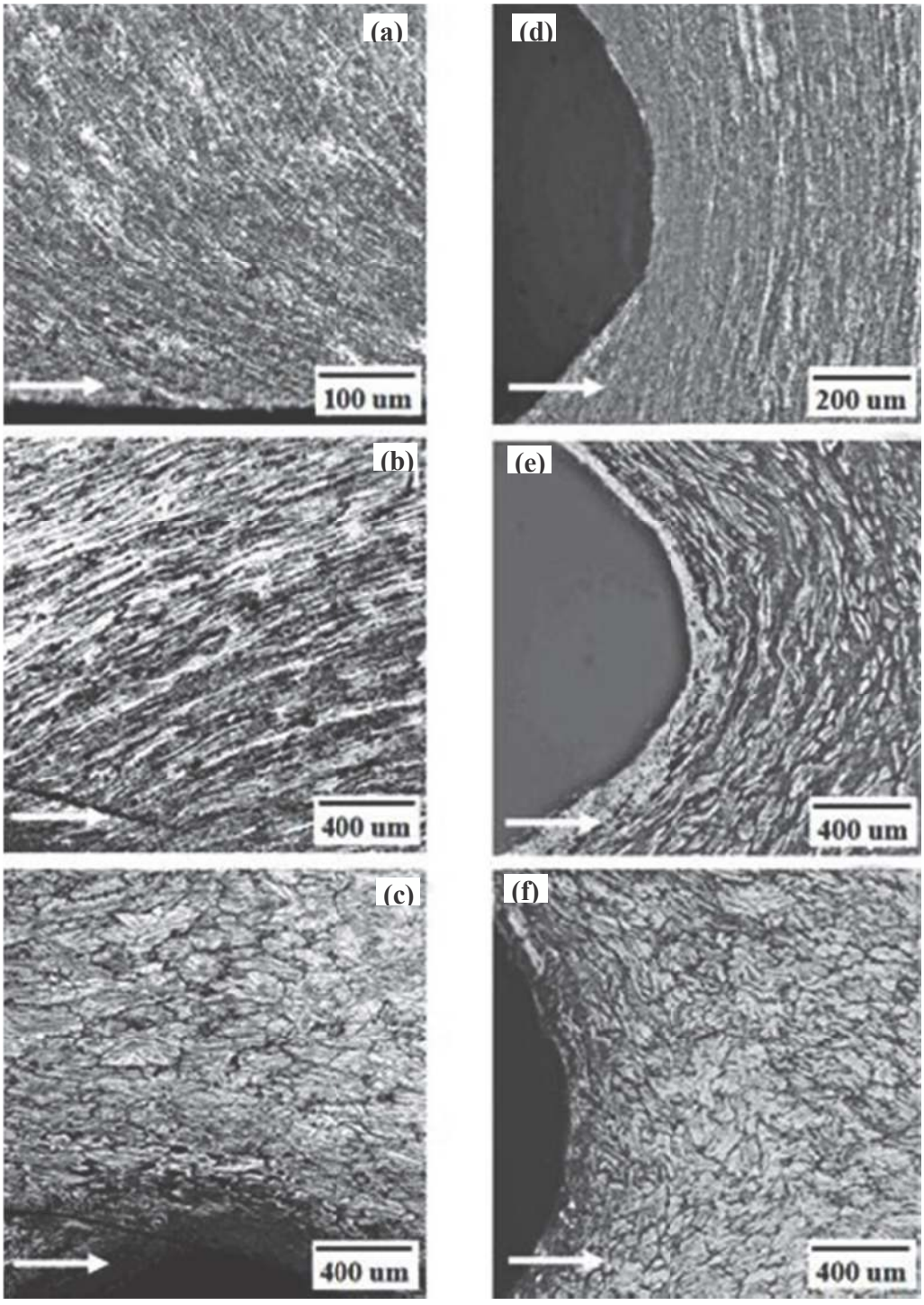

Fig. 4.10: Post ballistic microstructures adjacent to the crater wall of (a) ST, (b) LT, (c) L direction impacted plates; Post ballistic microstructure at the bottom of the crater of (d) ST (e) LT (f) L direction impacted plates; The arrow mark indicates the projectile penetration direction.

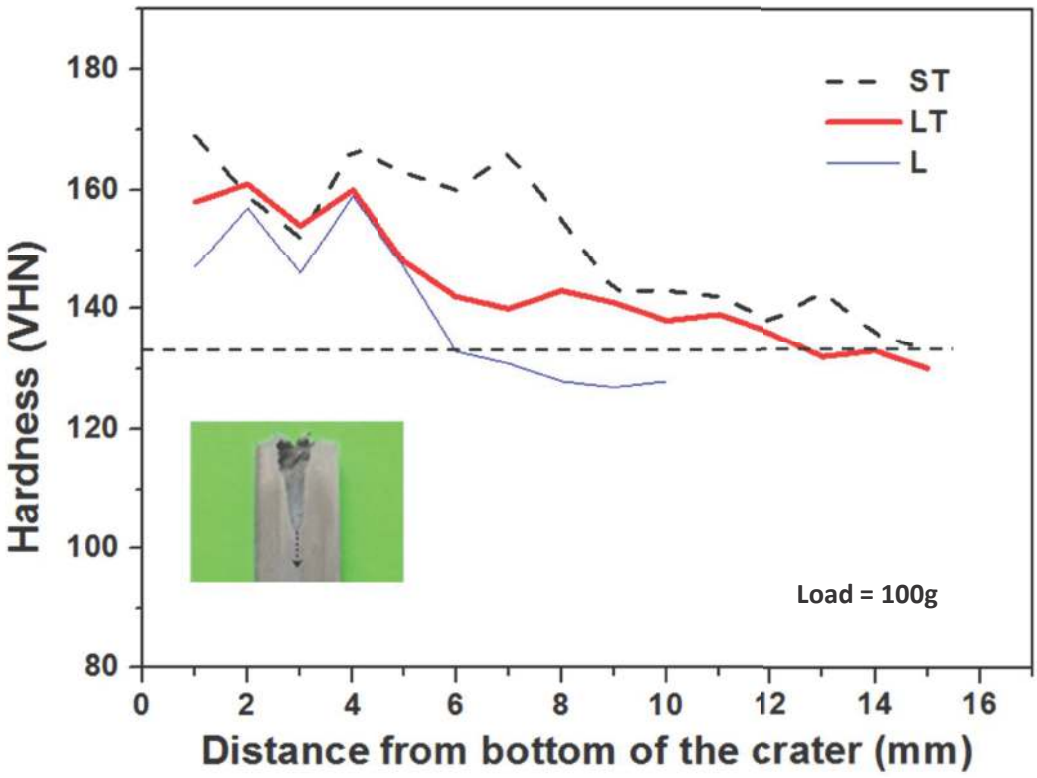

Fig. 4.11: Post ballistic micro-hardness measurements adjacent to the crater wall. The dotted line indicates the base hardness of the plate.

4.3. Discussion

The optical microstructures clearly reflect a difference in microstructure in the three directions of the AA-7017 plate. The plate exhibits equiaxed microstructure in ST while elongated grains are observed in L and LT directions (Fig.4.1a). Similar type of difference in microstructure in three directions has been reported in AA 7075 T651 alloy by Jordon et al. (2009). The microstructure in ST direction displays partial recrystallization around grain boundaries (Fig. 4.2b). The relatively large volume fraction of recrystallized grains in ST direction can be attributed to (i) temperature gradients produced through the work piece created by heat transfer between the rolls and the work piece and (ii) strain gradients created by friction between the rolls and the work piece (Chen et al.,2007).

The overall texture intensity along the three directions varies significantly. The texture components observed in ST are either recrystallisation component or located near recrystallization components. On the other hand, the texture in L and LT is quite sharp and close to typical Bs component. The corresponding β fibre also supports this observation. The variation in texture can be attributed to the difference in grain morphology along the three directions. Sharp texture observed in L and LT direction can be explained from the observation of highly oriented deformed grains along these two directions. In the same time, weak texture observed in ST direction is due to the presence of recrystallized grains.

The difference in the nature of mechanical properties anisotropy can be attributed to the microstructural constituents (grain size, morphology and distribution, associated crystallographic texture) present in the material. The plate displays highest strength value along LT, followed by ST and L direction. Similar observations in strength anisotropy have also been reported in AA-6061 alloy (Lee et al.,2014).

It is well known that the grain boundaries act as sink for the vacancies formed during rapid quenching from solution treatment temperature in the age hardening aluminium alloys. This results in the formation of precipitate free zones (PFZs) on both sides of the grain boundaries (Chen et al., 2009; Pedersen et al.,2011). Coarse intermetallic particles are also formed at the grain boundaries during quenching (Fig 4.1d). The PFZs and coarse intermetallic particles become regions for strain localization during deformation and hence the grain boundary region is weaker than the matrix in these alloys.

In addition, these alloys contain large amount of intermetallic particles inside the grains, which act as sites for the nucleation of voids. These voids can grow and coalesce to form a final crack. Therefore, the failure occurs as a result of the competition between two fracture mechanisms: intergranular fracture along the weak grain boundary regions and transgranular fracture by void formation at fine and coarse intermetallic particles within the grains. Due to the alignment of the grains, the amount of intergranular fracture surface varies in different directions. It is minimum and maximum for the specimens oriented along the L and ST directions. Since, the energy to create a crack is less along the grain boundaries, the ductility and impact energy is highest and lowest in L and ST direction, respectively.

The appearance of SEM fractographs of broken Charpy samples establishes the anisotropy in the fracture mechanism in three directions (Fig. 4.6a). In L and LT samples, dimples with transgranular cleavage facets dominate the fracture surface. The fracture surface of ST samples exhibits a failure mechanism influenced by the fracture of the constituent particle stringers. Once the constituent stringer particles are completely fractured, relatively large void like cavities formed and coalesced through the grain boundaries leading to an intergranular fracture. Presence of secondary cracks along the grain boundaries in case of L and LT samples and intergranular fracture in ST samples supports the presence of PFZ and intermetallic particles along the grain boundary.

The variation in ballistic behavior of the material in different directions can be explained from the microstructural and texture differences of the plate in three directions. Grain boundaries are weaker regions in this alloy as strain localization takes place easily around PFZ and coarse intermetallic particles. Hence, ballistic resistance of the surface with lesser grain boundary regions exhibits better performance. That's why the plate demonstrates better ballistic performance in ST direction impacted plates.

During ballistic impact, the projectile transfers its kinetic energy to the target material. Energy absorption in metallic materials takes place by plastic deformation. It has been reported that the diameter of the damaged region at the front face of an impacted anisotropic plate is less than that of the isotropic target (Radchenko et al., 1999). High intensity texture provides limited orientation of grains. It can therefore be inferred that the dissipation of projectile kinetic energy is constricted in L and LT directions due to the presence of high intensity texture. It has also been mentioned that a limited number of slip systems are activated for a material with a strong Bs texture (Chang et al., 1998). It implies that limited slip systems are available for the dissipation of the projectile kinetic energy when impacted in L and LT directions of the plate. This has introduced an inhomogeneous dissipation of energy during ballistic impact in L and LT directions. As a result, distorted material flow lines are observed after ballistic impact with high DOP values. On the other hand, weak texture in ST direction provides uniform distribution of dissipation energy. This has resulted in smooth material flow lines after ballistic impact adjacent to crater with low DOP value.

Observation of cracks in L and LT direction impacted target plates can again be corroborated with the weak grain boundary regions and sharp texture along these two directions. In the same time, observation of petals in ST direction impacted target plates points out that the impact energy is getting transmitted to the adjacent regions effectively. In contrast, partial broken petal damage pattern in the L and LT direction impacted targets suggest towards non uniform energy dissipation.

The ballistic behaviour of the material along three directions can be correlated very well with the post ballistic micro-structural observations of the impacted crater walls (Fig 4.10(a-e)). There is a visible difference in the microstructure at the bottom and adjacent to crater of the target plates impacted in different directions. It is noticed that in the ST direction impacted plates, smooth deformed material flow lines are observed at the bottom and adjacent to the crater wall. Whereas material flow lines are not detected adjacent to the crater wall in L and LT direction impacted target plates. Also heavily distorted grain structure is observed at the bottom of the crater in L and LT direction impacted target plates. Observations of material flow lines in the ST direction target plates indicate that a bigger volume of the material is associated in the deformation process. In the same time, comparatively lesser volume of material is involved in the deformation process of L and LT direction impacted plates.

The variation in hardness adjacent to the crater wall gives a good quantification of the material involved in the deformation process during projectile impact. The increase in hardness adjacent to the crater wall is caused by the strain hardening effect (Fig.4.11). In all the impacted target plates initially there is a rise in hardness. Beyond some distance, the hardness values gradually start to decrease until it reaches the initial hardness of the plate. The rise in hardness demonstrates the extent of strain hardening. Maximum extent of rise in hardness is observed in ST direction impacted target plates. This implies that the volume of the material involved in absorbing the kinetic energy of the projectile is higher in the ST direction impacted target plates. The micro-hardness results are therefore in accordance with the microstructural observations.

The present results provide a clear confirmation that the rolled AA-7017 alloy plate displays superior ballistic performance when impacted in ST direction. This is a result of

many contributing factors. Low aspect ratio pancake shaped grains lead to lesser strain localization. In addition, the projectile kinetic energy is distributed over a bigger volume due to overall weak texture in ST direction. This is confirmed from the observation of petals as well as absence of cracks in the front face of the ST direction impacted plates. Smooth material flow lines and larger extent of strain hardening adjacent to the crater walls also substantiate the participation of larger volume of material in the deformation process. Hence, each unit volume of material needs to absorb lesser amount of impacted kinetic energy. This enables the material to absorb the kinetic energy of the projectile in a homogeneous manner and enhances its ballistic performance. For better ballistic performance of any armor material, it is essential that it should be able to absorb the impacted energy of the projectile in a homogenous manner (Wingrove andWulf, 1973; Bhat, 1985).

Usually the ballistic behaviour of the material is correlated with static mechanical properties like strength, hardness and Charpy impact toughness (Übeyli et al., 2007; Dikshit et al. 1995; Jena et al., 2010b; Demir et al., 2008). In this study, it is observed that anisotropy exists in the quasi-static properties of rolled plates used for ballistic resistance applications. It is also noticed that the AA-7017 plate exhibits the best ballistic performance in ST direction, whereas it has moderate strength, lowest ductility and Charpy impact toughness along ST direction. It clearly points out that the ballistic performance of the material does not depend solely on its quasi static mechanical properties along the projectile impact directions. Instead the material properties in the lateral direction to the projectile impact also play a considerable role in ballistic performance.

4.4. Conclusions

There is a variation in morphology and orientation of the grains along three directions of the AA-7017 plate. This has resulted in anisotropy in mechanical properties and fracture behavior along three directions. The ballistic performance of the AA-7017 alloy plate is not concurrent with the quasi-static mechanical properties like strength, hardness, ductility and Charpy impact energy observed along three sample directions. Microstructure and texture appears to be a critical aspect for ballistic performance of the AA-7017 alloy plate. The grain boundary regions cause strain localization and are detrimental for ballistic performance.

Similarly, a strong texture inhibits the uniform dissipation of impact energy. Accordingly, the best ballistic performance is observed in ST direction of the AA-7017 plate as a result of the presence of less number of grain boundaries and a weak crystallographic texture. The post-ballistic microstructure and micro-hardness observations reflect the presence of nearly homogeneous deformation adjacent to crater wall of ST direction impacted target plates. It suggests that homogeneous deformation facilitates in uniform energy dissipation during ballistic impact and in turn enhances ballistic performance.